Steel slag powder as supplementary cementitious material in UHPC: influence on key properties and microstructure

Linbo Qiao[1], Xiaoxi Zhou[1], Han Deng[1], Bind Du[2]* and Ruilin Tang[3]

[1]Guizhou Provincial Mountainous Expressway Intelligent Operation and Maintenance Engineering Research Center, Guizhou Expressway Group, Guiyang, China, [2]College of Civil Engineering, Guizhou University, Guiyang, Guizhou, China, [3]Dundee International Institute, Central South University, Changsha, China

The large quantity of steel slag deposit has caused great environmental pressure. This study aims to recycle steel slag powder (SSP) as a supplementary cementitious material in the production of eco-friendly ultra-high performance concrete (UHPC) with varying SSP fineness (200−600 m²/kg) and dosage (20%−40%). The rheological properties, mechanical strength, autogenous/drying shrinkage, and microstructure of UHPC were systematically investigated using the Modified Andreasen and Andersen particle packing model. The results show that 20% SSP-400 optimally enhances compressive strength (133.5 MPa) by refining pore structure. SSP significantly mitigates autogenous shrinkage due to reduced self-desiccation, but increases drying shrinkage at high dosages/fineness (up to 21.5% at 40% SSP-600). Microstructural analysis confirms SSP-400 promotes complete hydration at 20%−30% dosage, while higher fineness accelerates early reactions but hinders later hydration. Ecological assessment validates SSP utilization reduces cement consumption and carbon footprint. Therefore, SSP-400 at 20% dosage enables sustainable UHPC with balanced performance.

1 Introduction

China, as the world's largest steel producer, generated approximately 104–155 million tons of steel slag in 2024, with nearly 70% disposed of via landfilling or stockpiling (Li Z. et al., 2025). This massive accumulation not only consumes valuable land resources but also poses severe environmental risks due to heavy metal leaching and dust pollution (Liu J. et al., 2025). Concurrently, Ultra-High Performance Concrete (UHPC) has emerged as a revolutionary cementitious material, characterized by ultra-high strength, exceptional toughness, and superior durability (Chen D. et al., 2025; Abutahnat et al., 2025). However, its widespread adoption is hindered by high production costs, primarily attributable to substantial cement and steel fiberconsumption (Çağlar, 2025). Additionally, UHPC exhibits pronounced autogenous shrinkagedue to its extremely low water-to-binder ratio, leading to

early-age cracking and compromised long-term durability (Chen M. et al., 2025). In order to enhance sustainability and reduce costs, there is an urgent need to explore new solutions utilizing industrial by-products such as steel slag powder (SSP) and fly ash (FA) as substitutes for additive material (Chen X. et al., 2025; Chen Z. et al., 2025). In particular, the mechanism by which steel slag affects the micro and macro properties of UHPC urgently needs to be clarified.

Many scholars have conducted research on the influencing factors of ultra-high concrete, especially SSP. As known that SSPs reactivity potential; its high CaO and MgO content enables alkali-activated geopolymer applications (Kim et al., 2025; Lan et al., 2025; Li J. et al., 2025). When used as aggregate, steel slag enhances mechanical properties and durability (Liu X. et al., 2025; Liu Z. et al., 2025), though its poor volume stability limits structural applications (Lou et al., 2025), often restricting its use to roadbeds or cement admixtures (Lü et al., 2025; Mohinderu et al., 2025). Micro-powder materials of SSP play a critical role in densifying concrete microstructure. By filling voids between aggregates, they improve particle gradation continuity (Onyelowe et al., 2025; Piao et al., 2025), increase density (Rahman et al., 2025; Smarzewski, 2025), and enhance strength, durability, and fire resistance (Smith et al., 2025; Song et al., 2025; Wang C. et al., 2025). However, regional shortages—such as limited FA availability in Panzhihua-necessitate composite admixtures combining FA with highly reactive alternatives like SSP (Wang T. et al., 2025; Wang Z. et al., 2025; Wu et al., 2025; Yue et al., 2025). Critically, utilizing these waste-derived materials reduces both costs and carbon emissions, as their recycling bypasses traditional clinker production burdens (Zhang B. et al., 2025).

In UHPC systems, SSP shows promise for improving flowability and mitigating drying shrinkage (Zhang C. et al., 2025; Zhao H. et al., 2025), yet systematic studies on its effects on rheology, mechanical properties, and autogenous shrinkage are scarce. The mechanisms governing SSP's role in shrinkage compensation and microstructural development remain poorly understood, particularly regarding interactions between SSP fineness, dosage, and curing regimes. Chemical expansion agents effectively reduce shrinkage but impair strength at high dosages (Zhao M. et al., 2025).

Therefore, it focused on the preparation of eco-friendly UHPC utilizing SSP as a supplementary cementitious material in this paper. SSP of varying fineness levels (200, 400, 600 m^2/kg) and dosages (20%–40%) was incorporated into the UHPC system. The rheological properties, mechanical strength development, and autogenous shrinkage behavior of SSP-enhanced UHPC were systematically investigated by DZS-1000 system, TT-LBY2 mortar rheometer and. XRD (X-ray Diffraction) and TG-DTG (Thermogravimetry-Derivative Thermogravimetry) were conducted to elucidate the underlying mechanisms of hydration, microstructure evolution, and shrinkage compensation. The study optimized SSP parameters to achieve eco-friendly UHPC with balanced performance. The results provide theoretical insights and technical pathways for enhancing the sustainability of UHPC through high-volume utilization of steel slag, offering significant economic and environmental benefits.

FIGURE 1
XRD of the steel slag powder.
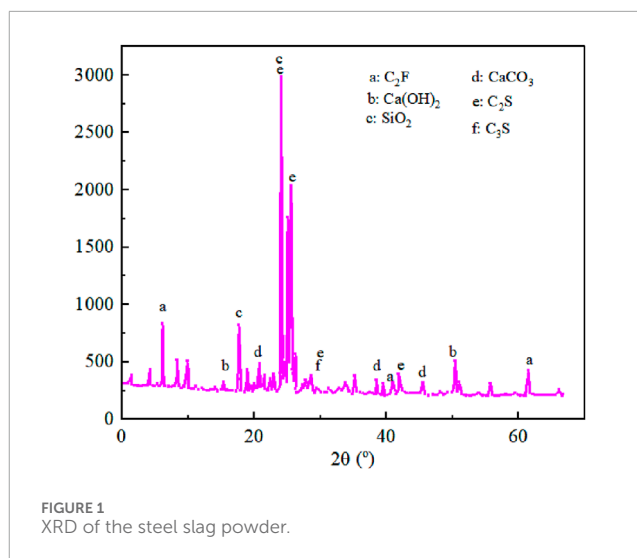
2 Materials and methods

2.1 Experimental materials

In this study, laboratory-formulated UHPC was used, which contains cementitious materials (P·O 42.5 silicate cement, silica fume, fly ash microspheres), aggregates (machine-made sand, fineness modulus 3.0), chemical admixtures (PCA®-1 polycarboxylic acid superplasticizer at 2% binder mass), and supplementary admixtures (steel slag powder as cement replacement). Hooked-end steel fibers (13 mm length × 0.22 mm diameter) were incorporated at 2% by volume (156 kg/m³), which meet the performance requirements of ASTM A820 for deformed steel fibers. The SSP was obtained by grinding industrial steel slag to three fineness grades, with Blaine fineness of 400 m^2/kg, 500 m^2/kg, and 600 m^2/kg respectively. The SSP used in this study is a grayish-black powder, with particle size distribution shown in Figure 1.

2.2 Specimen preparation and curing procedure

The UHPC specimens were prepared with SSP at replacement levels of 0%, 20%, 30%, and 40% of cement weight, designated as S0, U1S2, U1S3, U1S4 (for SSP-400), and similarly for SSP-500 (S2-series) and SSP-600 (S3-series). The mix design followed the Modified Andreasen and Andersen particle packing model, ensuring optimal density. The water-binder ratio was fixed at 0.18. Proportions are detailed in Table 1. After cleaning the mixer, dry constituents (cement, silica fume, SSP, and manufactured sand) were blended for 5 min. Steel fibers (2 vol%) were gradually added and mixed for 5 min to ensure uniform dispersion. Water and superplasticizer were then incorporated, followed by 5 min of wet mixing. The homogeneous mixture was cast into 50 mm × 100 mm molds, vibrated for 20 s to eliminate air bubbles, covered with plastic film, and cured at room temperature for 24 h. Specimens were demolded and transferred to standard conditions (20 ± 2 °C, RH

TABLE 1 Mixture proportion of UHPC mixed with SSP (kg/m^3).

Number	Cement	Sand	Water	Fibers	SSP-400	SSP-500	SSP-600	SF
U0	801	1,067	192	156	0	0	0	128
U1S2	641	1,067	192	156	160	0	0	128
U1S3	561	1,067	192	156	240	0	0	128
U1S4	481	1,067	192	156	320	0	0	128
U2S2	641	1,067	192	156	0	160	0	128
U2S3	561	1,067	192	156	0	240	0	128
U2S4	481	1,067	192	156	0	320	0	128
U3S2	641	1,067	192	156	0	0	160	128
U3S3	561	1,067	192	156	0	0	240	128
U3S4	481	1,067	192	156	0	0	320	128

>95%) for 28 days. For specific tests, steam curing (90 °C, 48 h) or natural curing (outdoor, 5–15 °C) was applied.

2.3 Test methods

This paper employs the DZS-1000 mechanical testing system to conduct mechanical tests, in order to determine the uniaxial compressive strength, strain and elastic modulus of ultra-high performance concrete. The rheological properties of mortar are tested using the TT-LBY2 mortar rheometer. Thermogravimetric analysis is performed with the German-made TG209F1LIbrahin. The mineralogical composition is analyzed using the Empyrean RAYON X-ray diffractometer. The main testing equipment and the testing procedure are shown in Figure 2.

2.3.1 Rheological performance testing

Rheological characterization was carried out on a TT-LBY2 mortar rheometer. Each 3 L batch was pre-sheared at 30 rpm for 60 s, rested for 60 s, and then subjected to a stepped shear-rate cycle (2 → 30 → 2 rpm) while torque and rotational speed were logged at 1 Hz. Down-curve data were fitted to obtain the Bingham parameters (yield stress τ_0 and plastic viscosity μ). All tests were completed within 10 min of mixing at 20 °C ± 2 °C. This was followed by a 60 s rest period to allow the material to stabilize. Subsequently, a stepped shear-rate cycle was applied, varying from 2 rpm to 30 rpm and back to 2 rpm. Torque and rotational speed were recorded at a frequency of 1 Hz throughout the test. All rheological measurements were conducted within 10 min after mixing under controlled temperature conditions of 20 °C ± 2 °C to minimize the influence of hydration.

2.3.2 Mechanical performance testing

The servo-controlled materials triaxial test system DSZ-1000 (Multi-field coupled rock mechanics testing machine) used in this study in Guizhou University. The main equipment includes a pressure device, a strut bar and support structure. The technical specifications of the machine are as follows: the maximum loading is 1,000 kN, and the force measuring range is 10–1,000 kN. Test force measurement accuracy is ≤ ± 0.5% FS. The maximum confining pressure is 60 MPa, and the confining pressure measurement accuracy is ≤ ± 0.25% FS. The axial strain gauge and radial strain gauge are fixed the anchor chain on the surface of the specimen and feed back to the measured strain information to the computer in time. In the test process, the specimen is subjected to axial deformation under the action of external loads, and the deformation of the sensor is converted into a signal through measurement, which is imported into the program of automatic strain calculation program.

2.3.3 Shrinkage performance testing

The rheological properties of the mortar mixtures were evaluated using a TT-LBY2 mortar rheometer. To ensure consistent and reproducible results, each freshly mixed 3 L batch was subjected to a standardized testing procedure. The sample was first pre-sheared at a constant rotational speed of 30 rpm for 60 s to disrupt any initial structural formation and ensure a homogeneous state. Autogenous shrinkage was assessed in accordance with ASTM C1698-09, using the corrugated tube method. Testing commenced at the initial setting time, which was identified based on mortar penetration resistance measurements. Data collection was performed automatically at hourly intervals for the first 72 h to capture early-age shrinkage kinetics. Ambient temperature and relative humidity were continuously monitored and recorded throughout both tests using HOBO MX2301A data loggers to ensure environmental consistency.

2.3.4 Thermogravimetric analysis testing

Thermogravimetric analysis (TGA) was performed to evaluate the hydration products and thermal decomposition behavior of UHPC samples. The specimens were first ground into a fine powder and then immersed in acetone for 7 days to effectively terminate hydration. After removal from the solvent, the powder was dried in

FIGURE 2
Testing equipment and procedures.

a vacuum desiccator and sieved through a 75 μm mesh to ensure uniformity. Approximately 20 ± 2 mg of the processed sample was loaded into an alumina crucible and tested under a nitrogen atmosphere. The temperature was programmed to increase from 30 °C to 1,000 °C at a constant heating rate of 10 °C/min. Continuous mass change recording allowed for the quantification of chemically bound water and identification of decomposition stages, particularly that of calcium hydroxide (CH), based on characteristic mass loss profiles.

2.3.5 Hydration microstructure testing

X-ray diffraction (XRD) analysis was conducted to identify the crystalline phases and monitor hydration products within the UHPC matrix. Sample preparation involved grinding hardened UHPC into fine powder followed by immediate immersion in anhydrous ethanol for at least 72 h to arrest hydration. The powder was subsequently vacuum-dried at 40 °C for 24 h to remove residual ethanol without altering phase composition. XRD measurements were carried out using a Bruker D8 Advance diffractometer with Cu-Kα radiation, operated at 40 kV and 40 mA. Scans were performed over a 2θ range from 10° to 80° with a step size of 0.02° and a counting time of 2 s per step. Phase identification was accomplished by comparing obtained diffraction patterns with reference databases.

3 Macro performance

3.1 Compressive strength

Figure 3 illustrates the influence of SSP fineness and dosage on the compressive strength of UHPC. Figure 3a depicts the effect of

SSP fineness. UHPC specimens incorporating SSP with a fineness of 200 m^2/kg achieved the highest compressive strengths across different dosages: 133.50 MPa, 124.90 MPa, and 129.20 MPa at 20%, 30%, and 40% replacement levels, respectively. At the 20% dosage level, SSP with finenesses of 200 m^2/kg and 400 m^2/kg yielded compressive strengths 3.35% and 0.55% higher, respectively, than the control group.

For 20% and 30% SSP dosages, the compressive strength exhibited an initial decrease followed by a slight increase as fineness increased, although the overall variation was minor. In contrast, at the 40% dosage, compressive strength gradually increased with higher fineness. This enhancement is attributed to the greater reactivity of finer SSP particles, which more effectively contribute to the micro-aggregate effect and pozzolanic reaction. This refines the pore structure, increases matrix density, and consequently boosts compressive strength.

For a given SSP fineness, increasing the dosage consistently led to a reduction in UHPC compressive strength. This occurs because higher SSP content reduces the cement fraction, diminishing the formation of hydration products essential for strength development. The most significant strength reduction occurred with SSP fineness of 200 m^2/kg, owing to its coarser particles and lower reactivity, which exerted the greatest negative impact. Specimens with 40% SSP (200 m^2/kg) exhibited a compressive strength of only 109.10 MPa, representing a 15.03% decrease compared to the control group.

Figure 4 presents the fitting curves depicting the relationship between SSP dosage and the compressive strength of UHPC at various fineness levels. It can be observed that for each fineness level, the compressive strength of UHPC decreases linearly with increasing SSP dosage. The correlation
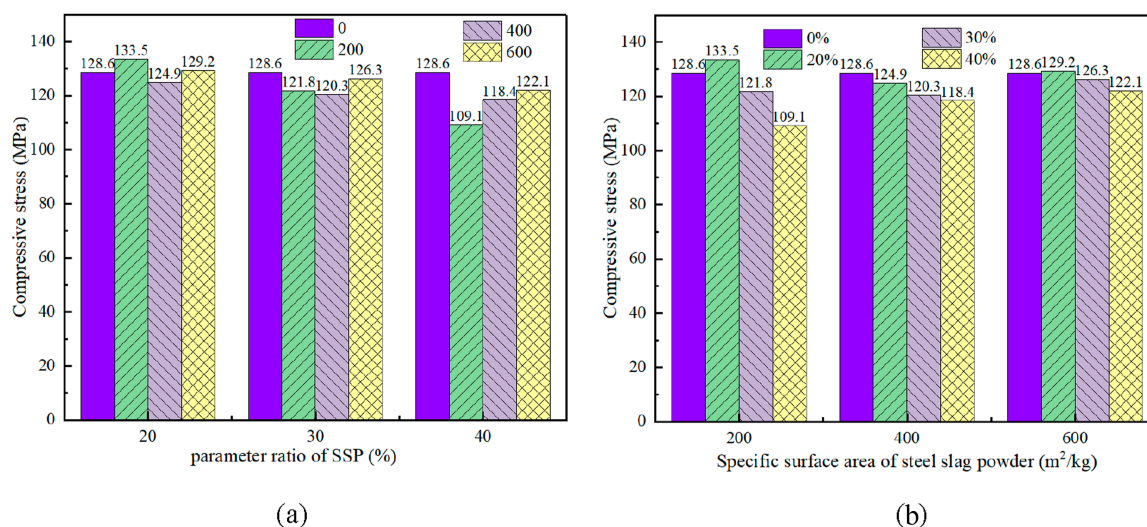
FIGURE 3
Effect of fineness and content of steel slag powder on compressive strength of UHPC. **(a)** Fineness of SSP. **(b)** Proportion of SSP.

coefficients (R^2) of the fitted linear functions all exceed 0.9, indicating strong linear correlations and excellent fitting performance.

3.2 Elastic modulus and microcracking

Figure 5 systematically investigates the influence of SSP fineness (200–600 m^2/kg) and dosage (20%–40%) on the axial compressive strength and elastic modulus of UHPC. The results reveal a pronounced threshold effect of SSP dosage on the mechanical properties of UHPC. At the 20% dosage level (S2 fineness group), specimen U3S2 exhibited axial compressive strength (125.7 MPa) and elastic modulus (43.9 GPa) marginally higher than those of the control group (U0: 124.2 MPa/ 43.8 GPa). This indicates that an appropriate dosage of high-fineness SSP optimizes matrix density through micro-aggregate filling and activation effects.

However, when the dosage increased to 30%–40%, both strength and modulus systematically deteriorated across all groups. For instance, at the 40% dosage, specimen U3S4 achieved a strength of only 103.8 MPa and a modulus of 39.8 GPa, highlighting the dominance of cement clinker dilution in driving performance degradation.

Fineness enhancement yielded benefits only at the 20% dosage. For example, U3S2 demonstrated a 5.4% higher strength than U1S2. Conversely, at the 30% dosage, even the finest S3 powder (U3S3, 600 m^2/kg) resulted in a strength (116.9 MPa) 6.0% lower and a modulus (42.1 GPa) 3.9% lower than the control group. This confirms that increased fineness only partially mitigates the adverse effects of high dosages.

Optimal performance requires the synergistic control of dosage (≤20%) and fineness (≥400 m^2/kg). Beyond this threshold, fineness improvement cannot compensate for the loss of rigid phases and interfacial weakening induced by increasing SSP dosage.

3.3 Drying shrinkage and mass stability

Figure 6 illustrates the influence of SSP fineness and dosage on the drying shrinkage of UHPC. The figure reveals that the development of UHPC drying shrinkage exhibits two distinct stages: An initial rapid phase (0–14 days) where shrinkage increases sharply, with the 14-day value accounting for over 75% of the total shrinkage at 60 days. This is followed by a decelerated phase (14–60 days) where the shrinkage rate significantly slows.

The experimental results demonstrate that only low-fineness SSP at the 20% dosage (specimens U1S2 and U2S2) exhibited a shrinkage-suppressing effect, reducing the 60-day shrinkage by 1.80% and 1.05%, respectively, compared to the control group. All other dosage groups, particularly high-fineness U3S3, exacerbated shrinkage. Notably, specimen U3S4 (40% dosage) showed a substantial increase of 21.53% in shrinkage relative to the control.

A critical observation is that the minimum shrinkage consistently occurred at the 20% dosage level. Conversely, within the 30%–40% dosage range, shrinkage systematically increased with higher SSP content. For example, in the S2 fineness group, shrinkage increased by 10.54% as the dosage rose from 20% to 40%. This trend is closely associated with the reduced hydration products and increased porosity induced by high SSP dosages.

Fineness plays a key regulatory role in shrinkage behavior: For any fixed dosage, higher SSP fineness consistently resulted in the greatest shrinkage. At dosages of 20%, 30%, and 40%, shrinkage exceeded the control by 11.72%, 19.88%, and 21.53%, respectively. This is attributed to the refinement of the pore structure by the micro-aggregate effect, which increases the proportion of fine capillaries and consequently amplifies the capillary tension stress driving moisture loss-induced shrinkage.

Interestingly, low-fineness SSP (U1S3) yielded the lowest shrinkage at the 30% dosage, while medium-fineness SSP (U2S4) performed best at the 40% dosage. Analysis of the fineness-dosage interaction reveals that the optimal shrinkage control
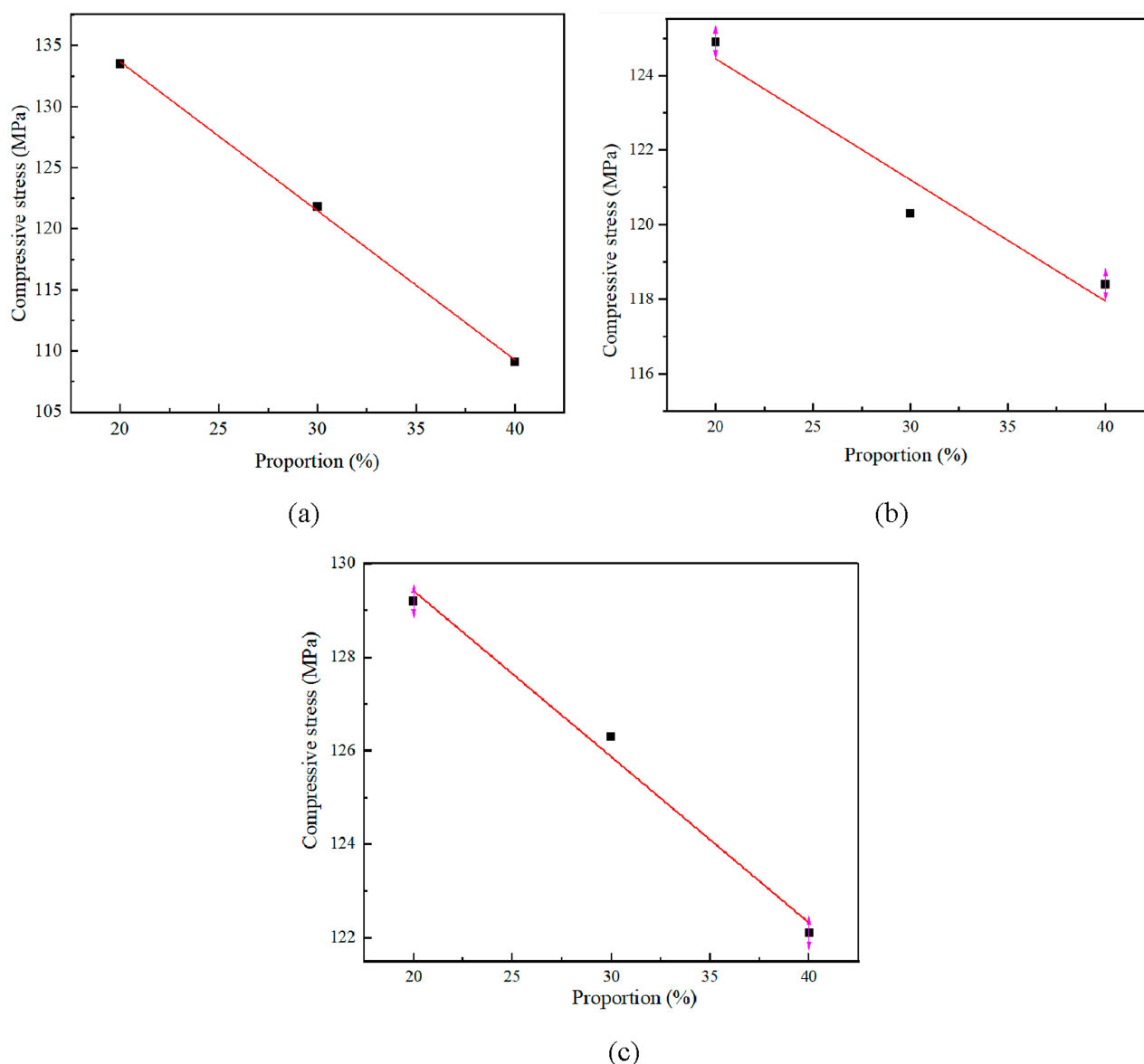
FIGURE 4
Relationship between SSP content and UHPC compressive strength. **(a)** 200 kg/m^2. **(b)** 400 kg/m^2. **(c)** 600 kg/m^2.

for any SSP fineness consistently occurs at the 20% dosage. At this level, the maximized formation of hydration products and minimized porosity effectively suppress moisture evaporation-driven shrinkage. Once the dosage exceeds 20%, shrinkage increases monotonically with SSP content, confirming that the cement dilution effect induced by high dosages dominates the degradation in shrinkage performance.

3.4 Autogenous shrinkage mitigation

Autogenous shrinkage in UHPC originates from the chemical shrinkage occurring during cement hydration. Following initial setting, the gradual formation of the hardened paste structure restrains volume changes, leading to the development of fine capillaries within the matrix. During this process, water extraction from coarse capillaries by fine capillaries induces self-desiccation. The resulting capillary underpressure-which Hua et al. [133] noted is inversely proportional to the radius of fine capillaries-generates tensile stress within the paste, ultimately manifesting as autogenous shrinkage.

This study employed the corrugated tube method to measure 72-h autogenous shrinkage. The initial setting time, determined by the mortar penetration test, served as the time-zero reference point, enabling precise differentiation between the contributions of chemical shrinkage (pre-initial setting) and self-desiccation-induced shrinkage (post-initial setting).

As shown in Figure 7, the incorporation of SSP significantly reduced the 72-h autogenous shrinkage of UHPC, with all tested groups exhibiting lower shrinkage than the control. The underlying
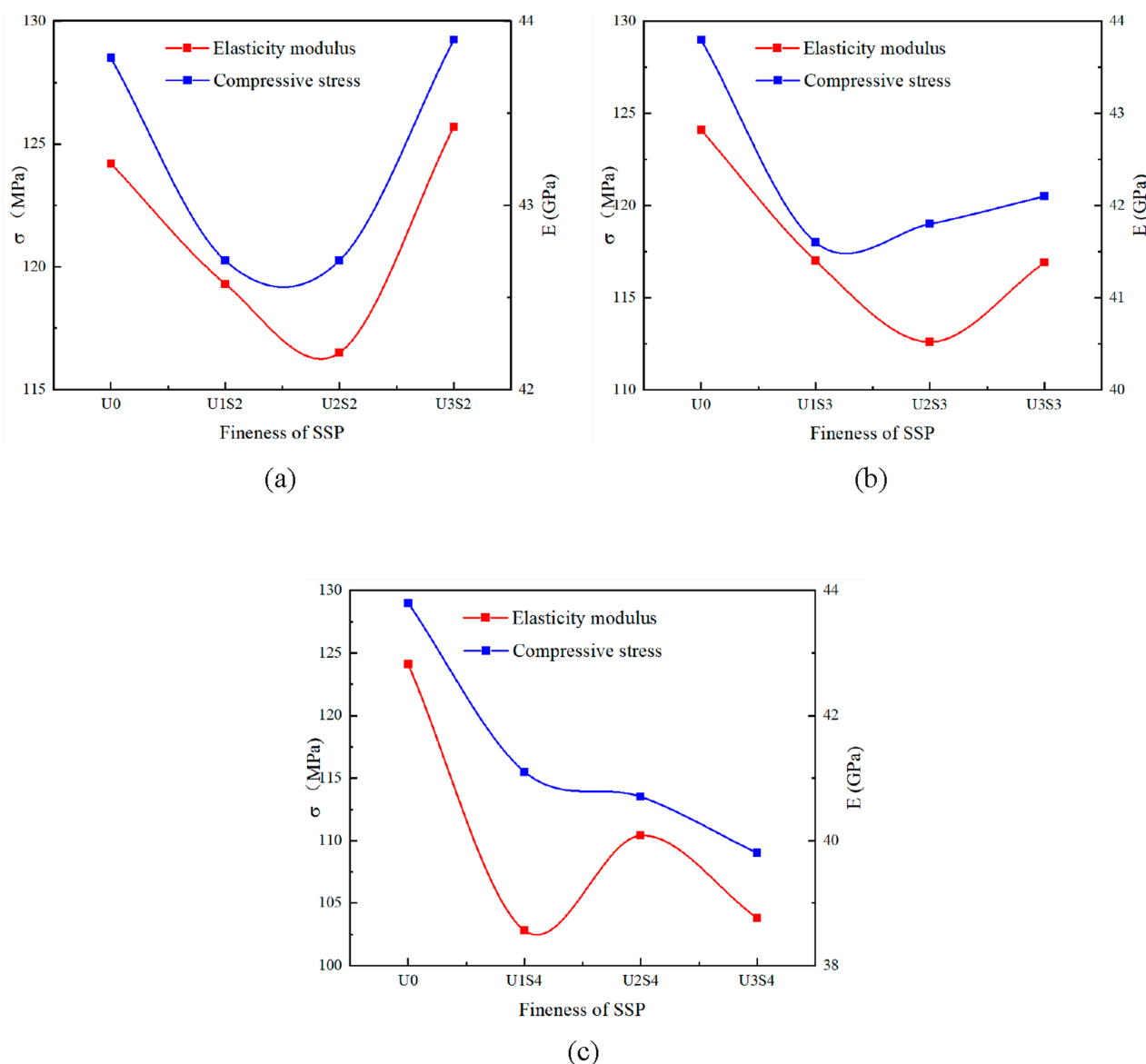
FIGURE 5
Effect of fineness and content of SSP on axial compressive strength and elastic modulus of UHPC. **(a)** 20% SSP. **(b)** 30% SSP. **(c)** 40% SSP.

mechanisms are twofold that the lower reactivity of SSP compared to cement reduces the overall early-age hydration degree of the binder system. The lower water demand of SSP increases the free water content in the mixture.

Analysis of fineness regulation revealed that low-fineness SSP provided the most pronounced shrinkage reduction. At dosages of 20%, 30%, and 40%, shrinkage was reduced by 22.05%, 30.78%, and 40.05%, respectively, compared to the control. This significant suppression is attributed to the coarser particle morphology (lowest fineness) of such SSP, which coarsens the paste microstructure and increases the proportion of coarse capillaries, thereby diminishing the capillary underpressure effect.

Regarding dosage regulation, autogenous shrinkage decreased monotonically with increasing SSP dosage for a given fineness. For instance, within the S1 fineness group, the 40% dosage exhibited

an additional 18% reduction compared to the 20% dosage. This trend stems from the further dilution of cementitious reactivity and the increased free water content, both of which alleviate self-desiccation stress.

4 Microscopic properties

4.1 X-ray diffraction analysis

Figure 8 presents the XRD patterns, revealing that distinct characteristic diffraction peaks of $3CaO \cdot SiO_2$ (C3S) and $2CaO \cdot SiO_2$ (C2S) persist in SSP-incorporated UHPC. This confirms the incomplete hydration of a portion of cement particles, providing a theoretical basis for utilizing SSP as a cement replacement in
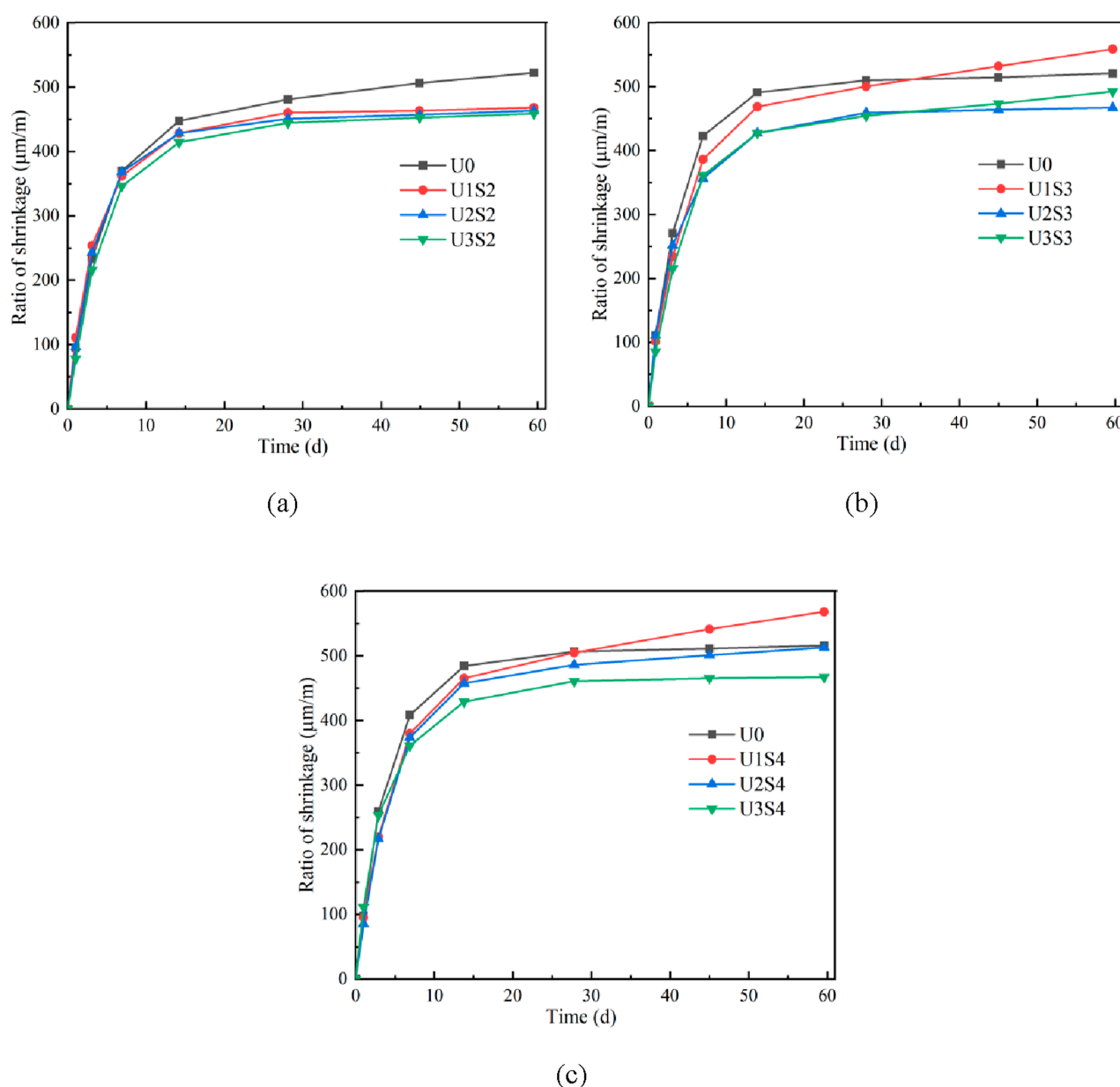
FIGURE 6
Effect of fineness and content of SSP on drying shrinkage of UHPC. **(a)** 20% SSP. **(b)** 30% SSP. **(c)** 40% SSP.

UHPC production. Notably, the inherent $Ca(OH)_2$ content within SSP led to higher $Ca(OH)_2$ peak intensities in some specimens (e.g., 20%–30% dosage S1/S2 groups) compared to the control group. The presence of larger $Ca(OH)_2$ crystals in these groups may potentially impair mechanical properties. Conversely, high-fineness SSP 600 exhibited the lowest $Ca(OH)_2$ and $Mg(OH)_2$ peak intensitiesacross all dosages, indicating insufficient formation of hydration products. This observation establishes a mechanistic correlation with the highest drying shrinkage observed for S3 groups in Figure 6.

Low-fineness SSP 200 at 20%–30% dosage promoted more complete C3S/C2S reaction, evidenced by significantly reduced silicate mineral diffraction peaks (decrease of 40%–50%) and enhanced formation of hydration products. The increased formation of C–S–H gel contributed to a more refined pore structure, which is directly linked to the densification of the matrix and the enhancement in compressive strength. This aligns with the superior compressive strength observed for these groups in Figure 5. However, at the 40% dosage, the SSP200 group showed increased intensity of unreacted C3S/C2S peaks, resulting in significant strength deterioration.

High-fineness SSP 600, due to its excessive refinement, accelerated early-age reactions, consuming substantial Ca^{2+} ions. This subsequently inhibited the formation of later-stage hydration products such as $Ca(OH)_2$ and ettringite (AFt), explaining its weakest shrinkage-suppressing capability observed earlier.

FIGURE 7
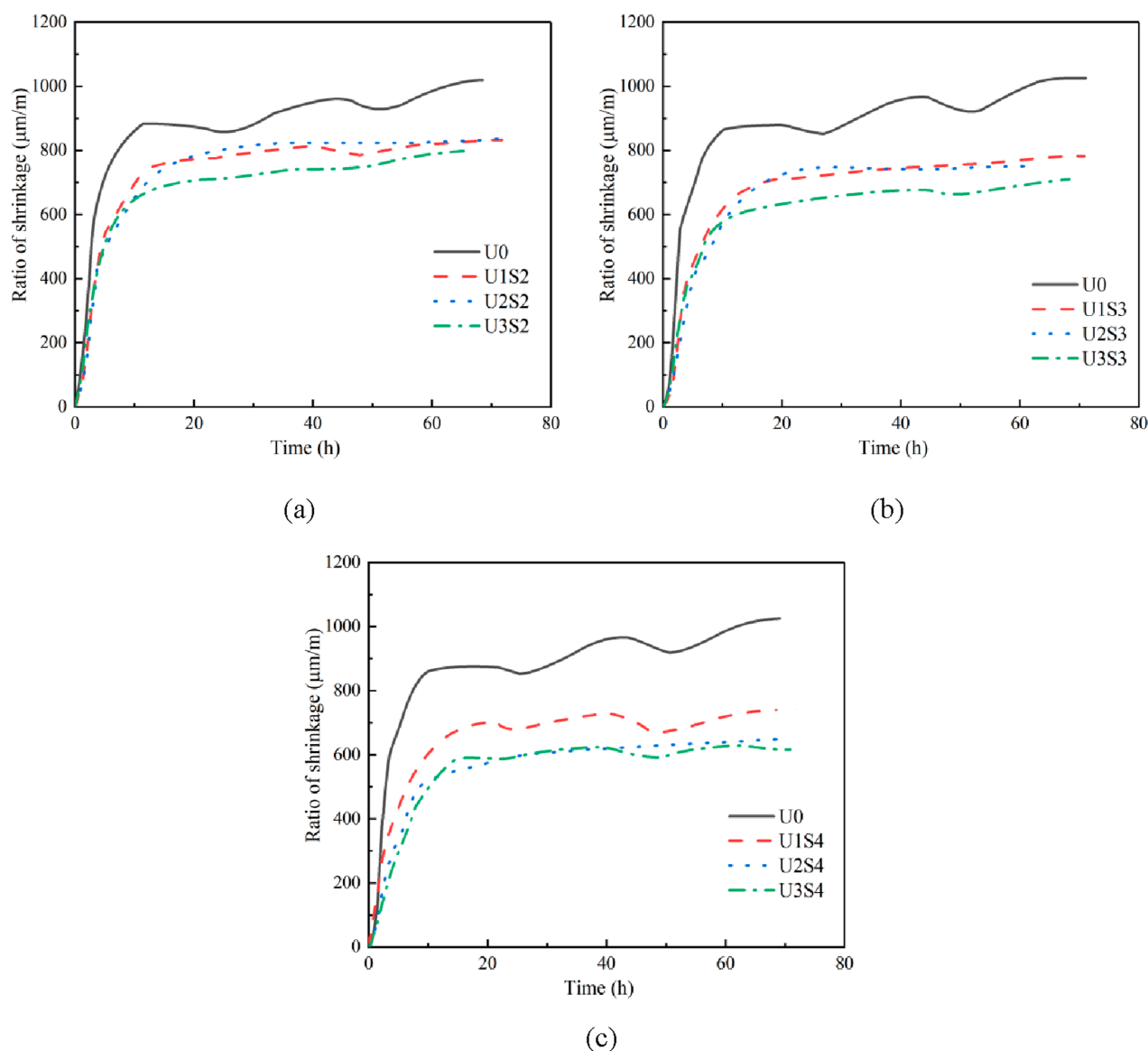Effect of fineness and content of SSP on autogenous shrinkage of UHPC. **(a)** 20% SSP. **(b)** 30% SSP. **(c)** 40% SSP.

Dosage effect analysis demonstrates that increasing SSP dosage systematically attenuated the characteristic peak intensities of $Ca(OH)_2$, $Mg(OH)_2$, and AFt. For instance, the $Ca(OH)_2$ peak intensity in the S2 group decreased by approximately 35% when the dosage increased from 20% to 40%. This reduction corresponds to a decrease in cementitious phasesand an increase in porosity. This finding not only explains the progressive decline in compressive strength with higher SSP dosage observed in Figure 5 (strength reduction ≥15% at 40% dosage), but also corroborates the micro-mechanism underlying the lowest drying shrinkage consistently observed for the 20% dosage groups in Figure 6 namely, sufficient hydration products effectively densifying the matrix.

The underlying mechanism can be attributed to the fact that coarser SSP particles (400 m^2/kg) provided nucleation sites that accelerated the hydration process. In contrast, finer particles with

a fineness greater than 400 m^2/kg increased agglomeration, which hindered the hydration process. This finding is consistent with previous studies that have shown the influence of particle size on the hydration kinetics and microstructural development of cementitious materials.

4.2 Thermogravimetric analysis

Figure 9 illustrates the influence of the fineness and dosage of SSP on the hydration heat evolution behavior of UHPC. As shown in the figure, the UHPC hydration heat evolution curve exhibits a typical five - stage kinetic process: the initial dissolution period (rapid reaction of C3A to form calcium sulfoaluminate), the induction period (slow dissolution of C3S leading to gradual
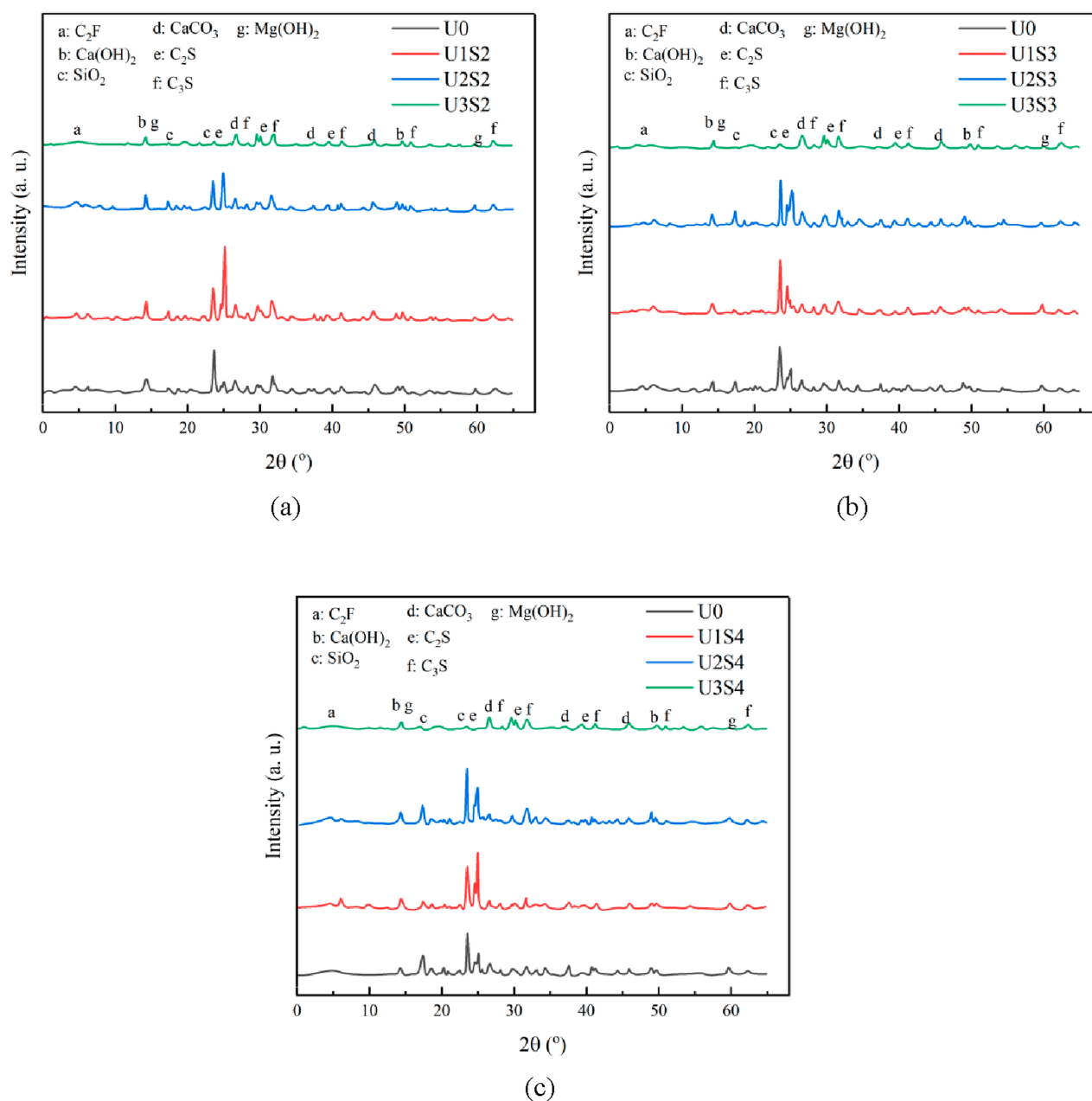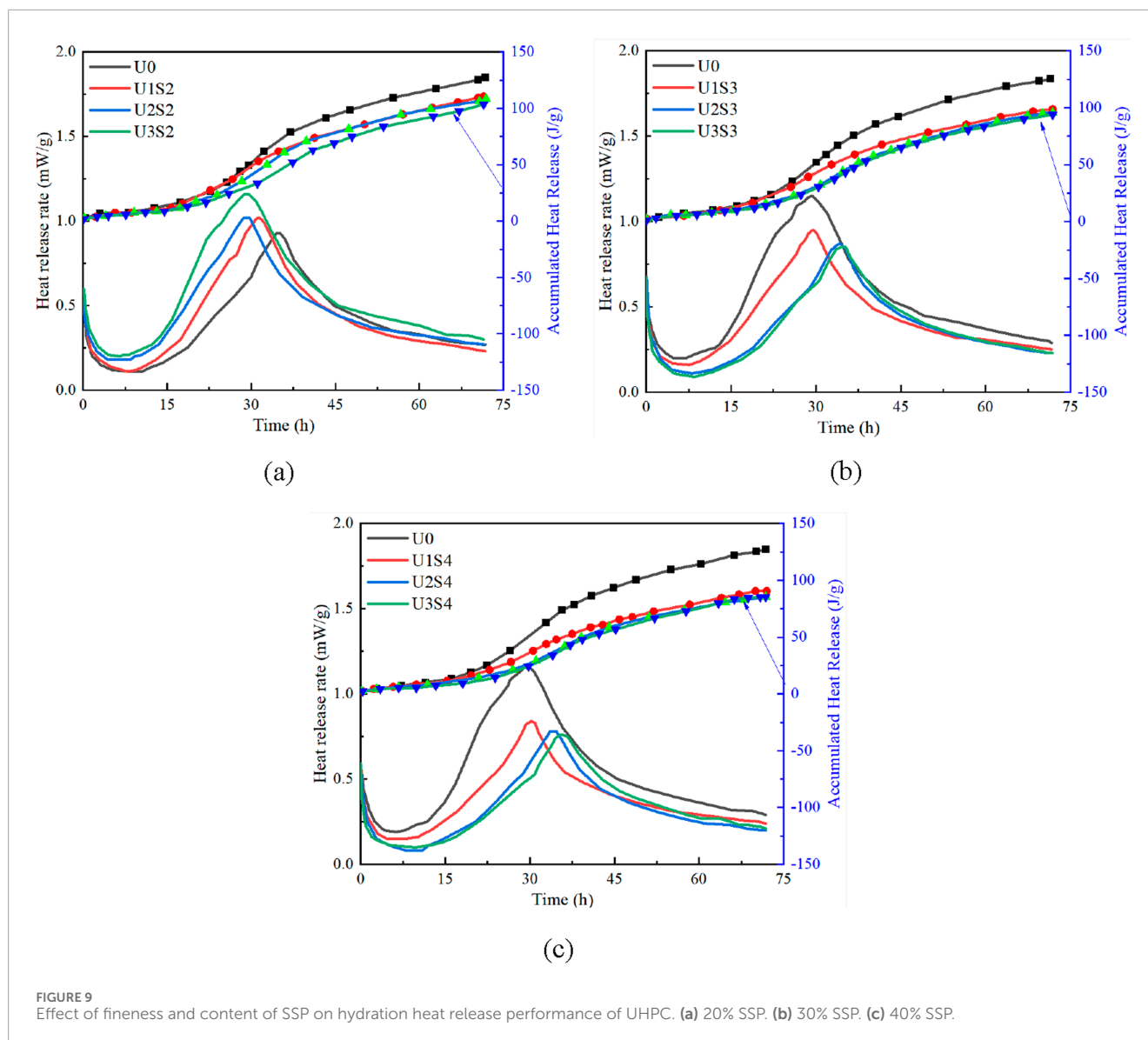
FIGURE 8
XRD pattern of UHPC mixed with SSP. **(a)** 20% SSP. **(b)** 30% SSP. **(c)** 40% SSP.

changes in Ca^{2+} concentration), the acceleration period (explosive hydration of C3S to generate C-S-H and $Ca(OH)_2$), the deceleration period (exhaustion of gypsum triggering the transformation of AFt to AFm), and the stabilization period (densification of hydration products inhibiting the reaction rate). The addition of SSP significantly reduces the intensity of the second exothermic peak and the total heat evolution after 72 h (all experimental groups are lower than the control group), confirming that it delays the hydration process by diluting the cement content and adjusting the reaction pathways.

The fineness - regulated analysis (Figures 9a–c) indicates that high - fineness powders (SSP600) can significantly enhance the hydration kinetics - the second exothermic peak of SSP600 occurs 20–30 min earlier than that of Group S1, and its peak intensity increases by 15%–20% (for example, at a dosage of 40%, the peak of SSP600 reaches 0.45 W/g, while that of S1 is only 0.37 W/g). This is attributed to the higher specific surface area, which enhances the reactivity of the particles. However, the total heat evolution of SSP600 after 72 h is only 3%–5% higher than that of SSP200, indicating that its accelerating effect is concentrated in the early stage.

More importantly, the delayed and reduced overall heat evolution in SSP-blended groups correlates well with the mitigation of autogenous shrinkage. The lower heat release indicates a

FIGURE 9
Effect of fineness and content of SSP on hydration heat release performance of UHPC. **(a)** 20% SSP. **(b)** 30% SSP. **(c)** 40% SSP.

slower hydration rate, which alleviates self-desiccation in the capillary pores—a primary cause of autogenous shrinkage in low-water/binder systems like UHPC. This provides a fundamental explanation for the reduced autogenous shrinkage observed in SSP-modified mixtures.

The dosage-regulated pattern reveals that, at the same fineness level, the intensity of the second exothermic peak and the total heat evolution systematically decrease with increasing dosage (for example, in Group SSP400, the peak intensity at a dosage of 40% is 32% lower than that at 20%, and the total heat evolution is reduced by 28%). This phenomenon is directly related to the cement dilution effect. It is worth noting that the group with a dosage of 20% always maintains the highest total heat evolution (for example, Group SSP200 reaches 285 J/g), which corresponds to the generation of more abundant hydration products to fill the pores. This explains the synergistic mechanism of the optimal compressive strength shown in Figure 5 and the lowest drying shrinkage rate shown in Figure 6 at the microscopic level. s. This explains the synergistic mechanism of

the optimal compressive strength shown in Figure 5 and the lowest drying shrinkage rate shown in Figure 6 at the microscopic level.

5 Conclusion

In this study, the mechanical properties, shrinkage behavior, and microstructural evolution of UHPC incorporating SSP were systematically investigated. Key conclusions are summarized as follows:

1. SSP fineness and dosage critically influence UHPC performance. A 20% cement replacement with SSP-400 (400 m^2/kg) achieves the optimal synergistic balance, yielding compressive strength (133.5 MPa) exceeding the control (129.2 MPa). This enhancement stems from SSP's micro-aggregate filling effect and latent hydraulicity, refining pore structure and increasing matrix density. Higher dosages

(≥30%) significantly reduce strength due to cement dilution and insufficient hydration product formation.

2. SSP incorporation effectively reduces early-age autogenous shrinkage, a major challenge in UHPC. Low-fineness SSP (400 m^2/kg) at 40% dosage achieves the maximum reduction (up to 40%). This is attributed to (i) reduced overall binder reactivity, lowering self-desiccation, and (ii) increased free water content. Higher dosages consistently reduce autogenous shrinkage for a given fineness.

3. While beneficial for autogenous shrinkage, SSP adversely affects long-term drying shrinkage, particularly at high dosages and fineness. Only low-fineness SSP (400 m^2/kg) at 20% dosage marginally reduced drying shrinkage (1.8%).

4. Coarser SSP (400 m^2/kg) promotes more complete silicate hydration (C3S/C2S consumption) at 20%–30% dosage, correlating with higher strength. Higher SSP dosages systematically reduce $Ca(OH)_2$, $Mg(OH)_2$, and AFt formation, increasing porosity and explaining strength loss and elevated drying shrinkage.

5. Utilizing 20% SSP-400 as a cement substitute in UHPC significantly enhances sustainability by valorizing a major industrial waste (steel slag), reducing landfilling and associated environmental risks. This substitution directly lowers cement consumption, reducing both production costs and the carbon footprint associated with clinker production.

Data availability statement

The original contributions presented in the study are included in the article/supplementary material, further inquiries can be directed to the corresponding author.

Author contributions

LQ: Writing – original draft, Funding acquisition, Data curation, Investigation, Writing – review and editing. XZ: Writing – review and editing, Supervision, Validation. HD: Formal Analysis, Writing – original draft. BD: Writing – original draft, Writing – review and editing, Investigation, Validation. RT: Methodology, Writing – original draft.

References

Conflict of interest

Authors LQ, XZ, and HD were employed by Guizhou Expressway Group.

The remaining authors declare that the research was conducted in the absence of any commercial or financial relationships that could be construed as a potential conflict of interest.

The authors declare that this study received funding from Guizhou expressway group Co., Ltd.. The funder had the following involvement in the study: Data collection and analysis.

Generative AI statement

The author(s) declare that no Generative AI was used in the creation of this manuscript.

Any alternative text (alt text) provided alongside figures in this article has been generated by Frontiers with the support of artificial intelligence and reasonable efforts have been made to ensure accuracy, including review by the authors wherever possible. If you identify any issues, please contact us.

Publisher's note

All claims expressed in this article are solely those of the authors and do not necessarily represent those of their affiliated organizations, or those of the publisher, the editors and the reviewers. Any product that may be evaluated in this article, or claim that may be made by its manufacturer, is not guaranteed or endorsed by the publisher.

Abutahnat, Y., Sorelli, L., and Refai, A. E. (2025). Tensile behavior of fiber-reinforced cementitious matrix with ultra-high-performance hybrid fiber-reinforced concrete (UHP-FRCM) with enhanced crack width control, fracture energy, and ultimate strength. *Constr. Build. Mater.* 489, 142430. doi:10.1016/j.conbuildmat.2025.142430

Çağlar, H. (2025). Finite element and experimental investigation of the inclined pull-out behavior of hooked-end steel fibers from carbon nanotube-reinforced ultra-high performance concrete. *Constr. Build. Mater.* 490, 142551. doi:10.1016/j.conbuildmat.2025.142551

Chen, D., Li, J., Shao, R., and Wu, C. (2025). Hydrogen/methane explosion loads and their effects on high-performance concrete: a comprehensive review. *Structures* 80, 109684. doi:10.1016/j.istruc.2025.109684

Chen, M., Chen, Y., Zhu, D., Kang, X., and Chen, R. (2025). Impact of stray current-induced steel fiber corrosion on the durability of ultra-high-performance concrete. *Constr. Build. Mater.* 489, 142386. doi:10.1016/j.conbuildmat.2025.142386

Chen, X., Zhang, L., Yu, H., Ma, H., Qiao, H., Yang, L., et al. (2025). Mechanical performance and durability evolution of high-performance concrete components exposed to Western salt lake environment. *Constr. Build. Mater.* 490, 142582. doi:10.1016/j.conbuildmat.2025.142582

Chen, Z., Liu, J., Zhu, F., Feng, K., and Boumakis, I. (2025). Experimental studies on pullout performance of anchor studs in high-performance concrete with hybrid steel fibers and synthetic fibers. *J. Build. Eng.* 111, 113380. doi:10.1016/j.jobe.2025.113380

Kim, S., Woo, S. Y., Piao, R., Banthia, N., and Yoo, D. Y. (2025). Synergistic effects of steel fiber surface treatments on the tensile performance of cementless ultra-high-performance alkali-activated concrete. *Cem. Concr. Compos.* 163, 106207. doi:10.1016/j.cemconcomp.2025.106207

Lan, T., Yang, S., Wang, Q., Chen, Z., and Wang, Y. (2025). Evaluation of dynamic fracture properties of ultra-high performance concrete: experimental study and analytical modelling. *Theor. Appl. Fract. Mech.* 139 (PA), 105055. doi:10.1016/j.tafmec.2025.105055

Li, Z., Shen, J., Zhu, H., Niu, G., Yang, L., and Gu, Z. (2025). Experimental study on the bond behavior of coarse aggregate ultra-high-performance concrete and HRB500 steel bars. *Constr. Build. Mater.* 490, 142446. doi:10.1016/j.conbuildmat.2025.142446

Li, J., Ma, Z., Shi, Y., Huang, Y., and Luo, Y. (2025). Compositional design of steel slag-based ultra-high performance concrete (UHPC) based on the D-optimal mixture design method: from macroscopic properties to microstructure (I). *Structures* 79, 109588. doi:10.1016/j.istruc.2025.109588

Liu, J., Cai, Y., Shi, F., Guo, C., Zhang, X., Li, S., et al. (2025). Fracture analysis of high-performance concrete impacted by abrasive water jet. *Powder Technol.* 465, 121326. doi:10.1016/j.powtec.2025.121326

Liu, X., Chen, Z., Yan, X., Chen, P., and Zhang, Y. (2025). Damage-rehydration synergy in strength evolution of ultra-high performance seawater sea sand concrete under marine tidal zones. *J. Build. Eng.* 111, 113358. doi:10.1016/j.jobe.2025.113358

Liu, Z., Qi, X., Ke, J., and Shui, Z. (2025). Enhancing the toughness of ultra-high performance concrete through improved fiber-matrix interface bonding. *Constr. Build. Mater.* 491, 142616. doi:10.1016/j.conbuildmat.2025.142616

Lou, C., Su, J., Zhao, X., Wu, D., Ma, J., and Li, Z. X. (2025). Eccentric pull-out test and numerical investigation of bond behavior of corroded high-strength steel bars in ultra-high performance steel fiber-reinforced concrete (UHPSFRC). *Eng. Struct.* 342, 120932. doi:10.1016/j.engstruct.2025.120932

Lü, C., Liu, D., Ding, Y., Lü, X., Zhou, Z., Mu, S., et al. (2025). Effect of early dry-wet cycles on the mechanical performance and microstructure characteristics of ultra-high performance concrete (UHPC) with varying metakaolin (MK) contents. *Constr. Build. Mater.* 490, 142471. doi:10.1016/j.conbuildmat.2025.142471

Mohinderu, K., Chadha, K., Pandey, D. K., and Bansal, P. P. (2025). An experimental investigation of confinement effectiveness of GFRP wrapping on beam-column joints retrofitted with high-performance hybrid fiber reinforced concrete. *Structures* 80, 109734. doi:10.1016/j.istruc.2025.109734

Onyelowe, K. C., Hanandeh, S., Ulloa, N., Barba-Vera, R., Moghal, A. A. B., Ebid, A. M., et al. (2025). Developing machine learning frameworks to predict mechanical properties of ultra-high performance concrete mixed with various industrial byproducts. *Sci. Rep.* 15 (1), 24791. doi:10.1038/s41598-025-08780-y

Piao, R., Woo, S. Y., Li, W., and Yoo, D. Y. (2025). Enhancement of mechanical and electrical properties of ultra-high-performance concrete through optimization of steel fiber aspect ratio and multi-walled carbon nanotube dosage. *J. Build. Eng.* 111, 113320. doi:10.1016/j.jobe.2025.113320

Rahman, M. N., Castro, S., Beheshti, M., Vedula, N. V., Noorvand, H., and Ozer, H. (2025). Development of a cyclic fracture experiment for characterization of high-performance asphalt concrete mixes. *Constr. Build. Mater.* 491, 142716. doi:10.1016/j.conbuildmat.2025.142716

Smarzewski, P. (2025). Mechanical properties and durability of ultra-high performance concrete containing steel fibers. *Compos. Struct.* 371, 119471. doi:10.1016/j.compstruct.2025.119471

Smith, A. S. J., Alshahrani, A., and Xu, G. (2025). Properties, damage law and stress-strain models for ultra-high performance fibre-reinforced concrete containing coarse aggregate. *Constr. Build. Mater.* 491, 142619. doi:10.1016/j.conbuildmat.2025.142619

Song, J., Banthia, N., and Yoo, D. Y. (2025). Effect of supplementary cementitious materials on durability of ultra-high-performance concrete: a review. *Cem. Concr. Compos.* 163, 106198. doi:10.1016/j.cemconcomp.2025.106198

Wang, C., Guo, T., Liu, L., Cheng, Z., Zhang, H., Huang, Y., et al. (2025). Fracture properties and reinforcement mechanisms of multi-scale hybrid fiber reinforced ultra-high performance concrete. *J. Build. Eng.* 111, 113436. doi:10.1016/j.jobe.2025.113436

Wang, T., Wang, Z., Yu, M., Sun, Z., and Xu, L. (2025). Fire resistance of ultra-high performance concrete-filled steel tubes slender columns at different concrete ages: experimental and theoretical investigation. *Eng. Struct.* 342, 120973. doi:10.1016/j.engstruct.2025.120973

Wang Z., Z., Sun, T., Sun, Y., and Liu, N. (2025). Evaluating the strength properties of high-performance concrete in the form of ensemble and hybrid models using deep learning techniques. *Sci. Rep.* 15 (1), 25453. doi:10.1038/s41598-025-10860-y

Wu, C., Li, H., Sun, R., Mou, B., Wang, X., Liu, Z., et al. (2025). Seismic performance of prefabricated RCS joints enhanced with ultra-high performance concrete. *Constr. Build. Mater.* 490, 142509. doi:10.1016/j.conbuildmat.2025.142509

Yue, R., Liu, Z., Wang, X., Xue, J., and Wang, J. (2025). Experimental study and calculation of carrying capacity for high strength steel reinforced ultra-high performance concrete column under eccentric compression. *Constr. Build. Mater.* 490, 142469. doi:10.1016/j.conbuildmat.2025.142469

Zhang B., B., Zhou, Y., Gong, H., Liang, Y., Liu, D., Wang, Y., et al. (2025). Effect of curing regime on ultra-high performance concrete containing metakaolin and magnesium oxide. *Constr. Build. Mater.* 490, 142388. doi:10.1016/j.conbuildmat.2025.142388

Zhang, C., Zhang, X., Wu, C., Yang, S., Yu, T., Wang, W., et al. (2025). Development of high performance and low-carbon red mud based lightweight concrete: a novel strategy for transforming red mud into sustainable concrete. *Constr. Build. Mater.* 491, 142714. doi:10.1016/j.conbuildmat.2025.142714

Zhao, H., Huang, H., Tang, J., Yao, C., and Gao, X. (2025). Thermal activation of lithium slag and its performance in ultra-high-performance concrete. *Constr. Build. Mater.* 491, 142682. doi:10.1016/j.conbuildmat.2025.142682

Zhao M., M., Hao, J., Xue, Q., Sun, X., and Fan, C. (2025). Axial compression behavior of ultra-high strength steel reinforced concrete columns confined by high strength spiral stirrups. *Constr. Build. Mater.* 491, 142620. doi:10.1016/j.conbuildmat.2025.142620